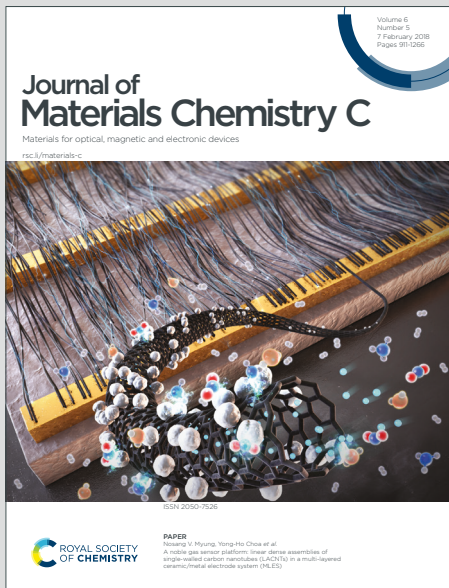


Journal of Materials Chemistry C

Materials for optical, magnetic and electronic devices

Accepted Manuscript

This article can be cited before page numbers have been issued, to do this please use: R. Venugopal, N. Ran, R. H. Blick, R. Zierold and J. Peng, *J. Mater. Chem. C*, 2026, DOI: 10.1039/D5TC03428K.



This is an Accepted Manuscript, which has been through the Royal Society of Chemistry peer review process and has been accepted for publication.

Accepted Manuscripts are published online shortly after acceptance, before technical editing, formatting and proof reading. Using this free service, authors can make their results available to the community, in citable form, before we publish the edited article. We will replace this Accepted Manuscript with the edited and formatted Advance Article as soon as it is available.

You can find more information about Accepted Manuscripts in the [Information for Authors](#).

Please note that technical editing may introduce minor changes to the text and/or graphics, which may alter content. The journal's standard [Terms & Conditions](#) and the [Ethical guidelines](#) still apply. In no event shall the Royal Society of Chemistry be held responsible for any errors or omissions in this Accepted Manuscript or any consequences arising from the use of any information it contains.

COMMUNICATION

Atomic-layer precision etching of SiO_2 using sequential molecular adsorption and plasma activationReceived 00th January 20xx,
Accepted 00th January 20xx

DOI: 10.1039/x0xx00000x

As device architectures in electronics, photonics, and quantum technologies scale reach atomic dimensions, precise and controllable material processing becomes essential. However, achieving atomic-layer precision in materials etching, even in silicon dioxide (SiO_2), remains a major challenge for next-generation nanofabrication. Here, we present a cyclic process that integrates sequential sulfur hexafluoride (SF_6) molecular adsorption with argon (Ar) plasma activation, enabling a stable etch-per-cycle (EPC) of $\sim 1.4 \text{ \AA}/\text{cycle}$ and 100% synergy between modification and removal steps. Mechanistic studies combining experiments, ab initio molecular dynamics, and density functional theory reveal that etching proceeds via a combination of reversible physisorption and defect-mediated chemisorption. Moreover, detailed morphology characterization over multiple cycles reveals a directional and uniform etching effect. This work introduces a scalable, contamination-free, precise etching strategy using standard reactive ion etching (RIE) equipment and commercially available gases, offering a robust and transferable platform for next-generation nanofabrication.

Introduction

Atomic layer processing technologies, most notably atomic layer deposition (ALD) and atomic layer etching (ALE), have emerged as key enablers for continued scaling of device architectures in electronics, photonics, and quantum technologies.¹⁻⁴ These techniques offer true atomic-level

control over material growth and removal, facilitating extreme dimensional precision, high aspect ratio features, and compatibility with three-dimensional integration. Their utility has extended into the fabrication of next-generation nanoelectronic systems, including quantum devices,⁵⁻⁹ all while remaining compatible with wafer-scale processing and high-volume manufacturing.¹⁰⁻¹² The concept of ALE was first introduced in a 1988 patent describing the cyclic removal of atomic layers from crystalline diamond via alternating nitrogen dioxide exposure and inert gas ion bombardment.¹³ At the time, limited demand for such precision constrained further development. However, as Moore's Law approaches its physical limits, ALE has gained renewed interest, particularly in advanced nanofabrication at the 10 nm technology node and beyond, where atomic-scale controllability, uniformity, and low damage are essential for enabling high-density integrated circuits, 3D NAND flash memory, and next-generation devices that require highly precise fabrication.^{11, 14} In 2015, Lee and George¹⁵ reported the first isotropic thermal ALE of Al_2O_3 , inspiring further exploration of atomic layer level precision etching techniques. Although etching of SiO_2 with atomic layer precision, one of the most basic semiconductor materials, has been tested by different etching strategies, it still remains challenging to keep control of accuracy and precision.¹⁶ Strategies using fluorocarbons (PFCs) or hydrofluorocarbons (HFCs) such as C_4F_8 , CHF_3 , CF_4 , have been leading the way. PFCs or HFCs are used to modify the SiO_2 surface to form a thin carbon-carbon film and subsequently Ar plasma bombardment is performed to remove the carbon-carbon polymer layer together with the SiO_2 thin layer. However, these etching approaches suffer from several drawbacks: polymer accumulation can destabilize the etch rate and uniformity; and residual carbon contamination can affect both the processing chamber and device surfaces. These issues likely contribute to the significant variability in reported EPC values, ranging from 1.9 to 27 $\text{ \AA}/\text{cycle}$ (Table S1). Consequently, other approaches, such as using trimethylaluminum and HF,¹⁷

^a Center for Hybrid Nanostructures, University of Hamburg, Luruper Chaussee 149, 22607 Hamburg, Germany. Email: jun.peng@uni-hamburg.de, robert.zierold@uni-hamburg.de.

^b State Key Laboratory of High-Performance Ceramics and Superfine Microstructures, Shanghai Institute of Ceramics, Chinese Academy of Sciences, 200050 Shanghai, China. Email: rannian@mail.sic.ac.cn.

^c DESY Photon Science Deutsches Elektronen-Synchrotron DESY, 22607 Hamburg, Germany.

† Supplementary Information available: [details of any supplementary information available should be included here]. See DOI: 10.1039/x0xx00000x



COMMUNICATION

Journal Name

¹⁸ plasma-involved processes with mixed precursors, or infrared-activated etching,¹⁹ are being actively pursued.

In this context, SF₆ presents a promising alternative due to its clean decomposition chemistry and absence of polymer-forming byproducts. In conventional etching processes, the use of SF₆ primarily relies on its plasma-phase dissociation into highly reactive fluorine radicals, which enables extremely fast etching rates, up to 1 $\mu\text{m}/\text{min}$,²⁰⁻²⁴ which introduces challenges in process control for precise etching. Here, we report a self-limiting, highly synergistic etching process for SiO₂ using sequential SF₆ gas exposure and Ar plasma etching near room temperature. Our process achieves a stable etch per cycle of \sim 1.4 $\text{\AA}/\text{cycle}$, with 100% synergy confirmed by decoupled half-cycle tests. Through systematic parametric studies, we identified both a temperature window and an ICP power window characteristic of ALE-like behavior. Mechanistic insights, supported by *ab initio* molecular dynamics and density functional theory calculations, reveal that the adsorption process in the etching proceeds via a combination of reversible physisorption and defect-mediated chemisorption. Notably, the process exhibits excellent directionality and maintains high uniformity across large areas, leveraging commonly available gases and existing commercial RIE equipment. This work introduces a practical, scalable, contamination-free, and potentially SF₆-recyclable etching strategy, which can be an important step toward precise nanofabrication in next-generation semiconductor and photonic devices.

Experimental

Etching and characterization

Si wafers with 285 nm wet thermally grown SiO₂ (SIEGERT WAFER GmbH) were cut into small pieces of approximately 1 cm \times 1 cm or 4.5 cm \times 4.5 cm for most etching experiments. In addition, SiO₂ layers deposited by ALD and plasma-enhanced chemical vapor deposition (PECVD) on Si substrates (SIEGERT WAFER GmbH) were etched as control samples. Details of the respective deposition processes can be found in our previous work.^{25, 26} Etching was carried out in a commercial ICP-RIE System (SENTECH SI 500). Film thickness was measured ex situ using an ellipsometer (SENTECH SENpro), with thickness values extracted using a Cauchy model for SiO₂. The film thickness was measured before and after etching. For pillar patterning, a positive electron beam resist (ARP661.09) was applied, and features were defined using an electron beam lithography system (Raith). The resulting sample was then subjected to a deep ion etching in the RIE system: At a continuous flow of 60 sccm SF₆, a plasma was generated with an ICP power of 300 W and a radio frequency (RF) bias of 60 W. The etching was carried out for 70 seconds. Then, the samples were cleaned with an Ar plasma of 300 W of ICP power for 120 seconds in the same RIE system. Surface morphology was characterized using scanning electron microscopy (SEM, Zeiss Crossbeam 550), and surface roughness was measured by atomic force microscopy (AFM, Dimension).

MD calculations

Ab initio molecular dynamics (AIMD) simulations were performed using non-spin-polarized²⁷ configuration, electronic energy convergence cut-off of 10⁻⁴ eV, a Γ -centered 1 \times 1 \times 1 k-point mesh, and a time step of 3 fs. The Perdew–Burke–Ernzerhof (PBE) functional within the generalized gradient approximation (GGA) were adopted as in the First-Principles Computation section. AIMD simulations were performed at 300 K using an NVT ensemble with a Nosé–Hoover thermostat for a duration of 30 ps, following structural relaxation.

DFT calculations

All DFT calculations were carried out using the projector augmented wave (PAW) method^{27, 28} in the Vienna *Ab initio* Simulation Package (VASP).²⁹ The exchange-correlation functional was described using GGA with the PBE parameterization. Convergence criteria were set to 10⁻⁵ eV for total energy and -0.05 eV/ \AA for forces. The plane-wave cutoff energy was set to 520 eV. The PAW pseudopotentials were VRHFIN = Si: s²p², VRHFIN = O: s²p⁴, and VRHFIN = F: s²p⁵. Gaussian smearing (ISMEAR = 0) with a smearing width SIGMA = 0.05 eV was applied. The Brillouin zone was sampled using a 2 \times 2 \times 1 Monkhorst–Pack grid for calculations involving surface defects on SiO₂ (001) surface. For electronic structure analysis, a denser 4 \times 4 \times 1 k-point grid was applied. The initial SiO₂ unit cell ($a = b = 4.91656 \text{ \AA}$, $c = 5.43163 \text{ \AA}$, space group P3₂21, No. 154, mp-6930) was constructed according to a Materials Project database.³⁰ The detailed computational model is shown in Figure S1. Long-range van der Waals interactions were accounted for using Grimme's DFT-D2 dispersion correction.

Results and discussion

1. Etching process and synergy characterization

The standard etching procedure follows a cyclic mode analogous to conventional ALE, as illustrated in Figure 1a. Each cycle comprises four steps: (i) *SF₆ exposure*: SF₆ gas is introduced into the reaction chamber at a flow rate of 20 sccm for 5 seconds, allowing a full modification on the surface. (ii) *Purge*: the SF₆ gas supply is stopped and the chamber is purged for 30 seconds. (iii) *Ar plasma etching*: an inductively coupled plasma (ICP) of Ar is ignited at 100 W for 60 seconds to perform the etching. (iv) *Cleaning purge*: the ICP is turned off, and the chamber is purged again for 30 seconds. In each cycle, steps (i) and (ii) constitute the modification half-reaction, while steps (iii) and (iv) constitute the removal half-reaction. This alternating half-cycle process yields a stable EPC \sim 1.4 $\text{\AA}/\text{cycle}$ (Figure 1b). Throughout the process, a continuous Ar flow of 100 sccm is maintained as a carrier gas, while the reactor is kept at room temperature and a working pressure of 1 Pa. Comparable EPC values, as shown in Figure S2, were obtained for SiO₂ deposited by ALD and PECVD using the same ALE recipe, indicating that the etching is predominantly surface-reaction-driven, with internal material defects exerting negligible influence. Figure 1c and Table S1 present a comparison of EPC values with previously reported ALE studies on SiO₂ over the past decade,^{19, 31-42} highlighting the superior precision of our "sequential SF₆ gas and Ar plasma" etching strategy. Notably, similar EPC values



were reproduced using the same recipe on a second, comparable RIE system, demonstrating the reproducibility and robustness of the method. Our process delivers EPC performance on par with thermal ALE but without the need for specialized equipment.

To gain a better understanding of the etching mechanism, control studies were performed by omitting either step (i) or (iii) from the standard etching cycle. First, the SF₆ gas input in step (i) was withdrawn, and the ICP power range in step (iii) was widened. No significant etching was observed (Figure 1d). This observation indicates that material removal in the standard process does not originate from Ar plasma-induced physical sputtering alone. Rather, it results from the synergistic interaction between the two half-reactions. In the ALE society, the degree of this synergy is quantitatively assessed using the ALE synergy factor, S , defined as:

$$S = \frac{EPC - (\alpha + \beta)}{EPC} \times 100\%$$

where α and β represent the apparent etch contributions from the isolated cycle of modification (steps i + ii) and removal (steps iii + iv) half-reactions, respectively, being undesirable etching.^{10, 43} As shown in Figure 1e and Figure 1f, repeating either half-reaction alone produces negligible etching, confirming that both α and β are effectively zero. Consequently, the synergy factor is calculated to be $S = 100\%$, indicating a fully synergistic process. This value exceeds that of previous ALE reports employing alternating fluorocarbon plasma and Ar ion bombardment, which achieved $\sim 80\%$ synergy in 10 nm logic device fabrication.⁴³ Note that the cyclic configuration that separates SF₆ exposure and Ar plasma etching steps is critical to maintaining the precise etching behavior. As the tests shown in Table S2, mixing the SF₆ and the Ar during the plasma step, either cyclically or continuously, yields significantly higher EPC values, resembling a reactive ion etching (RIE) process.

2. Etching characteristics

Comparative analysis of various etching strategies suggests that our “sequential SF₆ gas and Ar plasma” method follows strictly neither RIE nor ALE characteristics but is closer to a combination of both. To validate this assumption, a series of systematic experiments were conducted to assess the process behavior under varying parameters. Figure 2a shows the effect of wafer holder temperature on the etching rate. Between room temperature and approximately 40 °C, the EPC remains stable, defining a distinct temperature window for optimal etching. Beyond this range, up to 160 °C, the EPC gradually decreases, which is likely due to increased thermal energy causing SF₆ molecules to desorb more easily from the surface, thereby reducing their availability for effective surface modification. In addition to the temperature window, a working pressure window was also identified (Figure 2b). As the pressure increased to 0.8 Pa, the EPC increased to 1.4 A/cycle sharply; then, until 8 Pa, the EPC remained at a plateau. However, with further increases in pressure, the EPC begins to rise again. This behavior may be attributed to insufficient purge time at higher pressures, allowing excessive SF₆ molecules to persist in the

chamber. Note, there is no sputtering etching within the testing pressure if the step (i) SF₆ exposure is absent¹¹ (Figure S3). Upon plasma ignition, these residuals generate additional F radicals for etching. Figure 2c presents the EPC dependence on ICP power. In general, higher ICP power results in increased gas ionization and ion density (Figure S4). However, the EPC curve, which first increases and then decreases with increasing ICP power, mirrors the trend of Ar plasma ion energy as measured on identical equipment (Figure S4). This correlation suggests that ion energy, rather than ion density, is the dominant factor influencing etching in the tested 0–700 W range. The relatively flat EPC result within the 50–100 W range likely corresponds to an “etching window,” where the incident plasma ion energy is sufficient to remove the SF₆-modified surface layer without damaging the underlying SiO₂. Below this energy threshold, incomplete removal of the modified surface leads to reduced EPC. As shown in Figure 2d and Figure 2e, as the SF₆ exposure time in step (i) and the plasma etching time in step (ii) increase—corresponding to an increase in dose—the EPC saturates at an EPC ~ 1.4 Å/cycle. The above behaviors are consistent with the self-limiting saturation characteristic expected in ALE processes. However, when the purge time following the SF₆ exposure (step (ii)) is extended, the EPC does not remain constant as expected. Instead, it drops quickly and ultimately approaches zero etching, as shown in Figure 2f. This result indicates that the modification half-reaction is reversible, deviating from the typical ALE working principle derived from the ALD concept, which assumes irreversible surface reactions.⁴⁴ Furthermore, the shape of the EPC–purge time curve implies that the adsorption behavior in the modification step is governed predominantly by reversible type I physisorption,⁴⁵ rather than chemisorption.

However, an etching process whose modification half-reaction is dominated by reversible saturated physisorption, exhibits an ICP power window (Figure 2c) comparable to the temperature window typically observed in ALE/ALD processes governed chemisorption. This phenomenon is counterintuitive. To clarify this behavior, simplified SiO₂ surface models terminated with either Si or O atoms (Figure S1) were constructed to exam the adsorption behavior of SF₆. *Ab initio* molecular dynamics (AIMD) simulations (Figure S5, Video S1, and Video S2) reveal that Si-terminated surfaces can chemisorb and partially dissociate SF₆ molecules, whereas O-terminated surfaces remain inert and exhibit negligible adsorption. DFT calculations (Figure S6) further show that SF₆ adsorption on Si-terminated surfaces has an adsorption energy E_{ads} of -5.98 eV, indicative of strong chemisorption, with F atoms forming stable Si–F bonds with exposed Si atoms. In contrast, adsorption on O-terminated surfaces exhibits a much weaker E_{ads} equals to -0.22 eV, without the formation of stable chemical bonds. These results confirm that the modification half-reaction involves a combination of chemisorption and physisorption, consistent with experimental observations: the ICP power window (Figure 2c) reflects chemisorption behavior, while the EPC–purge time dependence (Figure 2f) represents physisorption dynamics. Moreover, an etching process using only pulsed SF₆ plasma



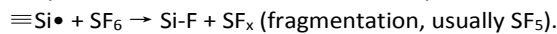
COMMUNICATION

Journal Name

(Table S3) yielded an EPC of 0.5 Å per cycle, approximately one-third that of the standard ALE process, indicating that chemisorption contributes only partially to the overall adsorption. This demonstrates that, although our process achieves atomic-level etching precision, it does not conform to a purely conventional ALE mechanism.

3. Etching mechanism exploration

Next, the SiO_2 surface defect sites as potential active adsorption centers for SF_6 are explored. At room temperature, the SiO_2 surface hosts various stable or metastable defects, with the most prevalent being silicon dangling bonds ($\equiv \text{Si}\bullet$), oxygen-centered radicals ($\equiv \text{Si}-\text{O}\bullet$), doubly coordinated silicon radicals ($=\text{Si}\bullet$), and strained siloxane rings (Si_2O_2).⁴⁶⁻⁴⁸ Density functional theory (DFT) simulation was used to construct and relax these defect structures under vacuum at room temperature. Among them, three were found to be thermodynamically stable: $\equiv \text{Si}\bullet$, $\equiv \text{Si}-\text{O}\bullet$ and Si_2O_2 rings, as shown in Figure 3a. F atoms were sequentially introduced to these defect sites, and the corresponding adsorption energy E_{ads} was calculated. All three sites exhibit negative E_{ads} values, indicating spontaneous and energetically favorable formation of Si–F bonds. In the etching cycles, F atoms can originate from two potential primary sources: First, the spontaneous dissociation of SF_6 at defect sites during step (i), and second, the plasma-induced dissociation of physically adsorbed SF_6 during step (iii). For the former origin, a thermodynamically favorable chemical reaction occurs only if E_{ads} exceeds the dissociation energy E_{diss} of SF_6 into SF_5 and F, which is calculated to be 3.03 eV. For example, the chemisorption at $\equiv \text{Si}\bullet$ defect sites can be expressed as:



As shown in Figure 3b, among the studied defects, only the Si_2O_2 ring possesses a sufficiently negative E_{ads} to overcome E_{diss} , thereby providing enough energy, and enabling spontaneous dissociation of SF_6 and subsequent F adsorption. The other defects exhibit insufficient E_{ads} , which aligns with the experimental observation that the overall surface behavior is dominated by physisorption (Figure 2f). For the latter sources, plasma-activated Ar^+ ions dissociate physically adsorbed SF_6 , generating free F radicals, which can spontaneously react with defect sites to form stable Si–F bonds. Crystal orbital Hamilton population (COHP) analysis⁴⁹ was used to compare the related bond strengths E_b as a function of F adsorption. As shown in Figure 3c, after adsorbing F atoms, the Si–O bond strengths $E_{b, \text{Si}-\text{O}}$ at the defect sites decrease. The Si–O bonds at $\equiv \text{Si}-\text{O}$ and Si_2O_2 rings with single F adsorption, and $\equiv \text{Si}\bullet$ with two F adsorptions, exhibit lower Si–O bond strength $E_{b, \text{Si}-\text{O}}$ than the Si–O bond strength in defect-free regions $E_{b, \text{Si}-\text{O}, \text{normal}}$. This implies that, under Ar plasma bombardment, the weaker Si–O bonds near Si–F sites are more preferentially broken than the Si–O bond in defect-free regions. Therefore, when the incident Ar ion energy is larger than $E_{b, \text{Si}-\text{O}}$ but smaller than $E_{b, \text{Si}-\text{O}, \text{normal}}$, the etching is highly controllable and only limited to the surface, similar to pure ALE processes. This supports the existence of an "etching window" (Figure 2c), in which the energy of incident Ar^+ ions falls between $E_{b, \text{Si}-\text{O}}$ and $E_{b, \text{Si}-\text{O}, \text{normal}}$ — sufficient to break the Si–O bonds that are

modified and weakened by Si–F bonds but insufficient to sputter the unmodified and defect-free surface regions. Note, when the ion energy exceeds $E_{b, \text{Si}-\text{O}, \text{normal}}$, the surface will be etched by physical sputtering.

Based on these findings, the etching mechanism for this four-step cyclic sequence is proposed in Figure 3d. In step (i) SF_6 exposure, most SF_6 molecules are physically adsorbed onto the SiO_2 surface, and only a small amount of SF_6 molecules can be dissociated at high-reactivity defect sites, e.g., Si_2O_2 rings, forming Si–F bonds. None of the adsorption produces an etching effect. And the physical adsorption remains the dominant interaction. In step (ii) Purge, excess SF_6 is removed, and the adsorbed SF_6 amount on the surface can be tuned by adjusting purge duration or chamber pressure. In step (iii) Ar plasma etching, the plasma dissociates physisorbed SF_6 and F radicals are produced, which react with surface defects to form Si–F bonds. Simultaneously, Ar^+ ions provide energy to cleave weakened Si–O bonds adjacent to the Si–F bonds. The fluorinated Si atoms then further react with radicals to form volatile byproducts.^{50, 51} Finally, the volatile by-products are evacuated in step (iv) Cleaning purge, preparing the surface for the next cycle. It is worth noting that most conventional etching schemes utilizing SF_6 , the entire gas flow is converted into plasma, and fluorine radicals generated through ionization or fragmentation act as the primary etching species. In contrast, in our process, only the absorbed SF_6 molecules are fragmented to participate in etching, while the unadsorbed fraction remains intact and is purged as stable SF_6 molecules during the modification half-reaction. These unreacted molecules can potentially be captured, compressed, and recycled, significantly reducing process emissions. Although the use of SF_6 , a potent greenhouse gas, cannot be entirely eliminated, our etching approach achieves lower gas consumption and improved environmental compatibility, thereby offering a more sustainable pathway for precision plasma etching.⁵²⁻⁵⁴

4. Directional etching

Validating the directionality — directional or isotropic — of this etching process determines how this process can be used in advanced patterning applications. To assess this, a SiO_2 substrate patterned with cylindrical pillars of 600 nm diameter was used. Optical microscope images (Figure 4a) were captured after various etching cycles. The observed color variations in the optical images reflect changes in SiO_2 film thickness due to material removal. The corresponding atomic force microscope (AFM) images (Figure 4b) and detailed interface profile (Figure 4c) show, however, no significant difference after each etching process. These results reveal that the surface morphology of the pillars remains essentially unchanged throughout the etching cycles. Specifically, the sidewalls of the pillars retain their shape, indicating that the etching is anisotropic and proceeds primarily in the vertical direction (Figure 4d). In contrast, isotropic etching should reduce both the height and diameter of the pillars uniformly, as sketched in Figure S8. Quantitatively, the total etched depth was approximately 62 nm (Figure 4e) corresponding to the determined 1.4 Å/cycle, while the pillar



diameter remained constant. If the process would have been isotropic, the pillar diameter would have decreased by an estimated 27%. This preservation of lateral dimensions strongly supports the directional nature of the etch. The observed anisotropy is likely driven by a bias voltage generated unintentionally during Ar plasma pulses, potentially due to the self-bias effect and capacitive coupling from the ICP power supply. Although no deliberate RF bias was applied, a passive bias was detected during plasma ignition (Figure S9). This bias establishes an electric field in the plasma sheath, accelerating charged particles, primarily Ar^+ ions, perpendicularly toward the substrate. As a result, the etching becomes angle-selective: ions arriving at high incident angles possess lower kinetic energy, making them less likely to erode sidewalls or lateral features.^{55, 56} Additionally, the low operating pressure ensures a large mean free path, further promoting unidirectional ion trajectories and reinforcing vertical etch selectivity. This directional etching behavior was also consistently observed in hole-patterned samples (Figure S10), indicating excellent repeatability on different nanostructured geometries. Surface characterization after etching confirmed the gentle nature of the process, with an unchanged post-etch surface roughness (Ra) of approximately 0.7 nm. Moreover, large-area uniformity tests on 4.5 cm \times 4.5 cm wafer showed an etching uniformity of 3.96% after 150 cycles (Figure S11). It is well below the $\pm 5\%$ threshold typically required by the semiconductor industry for dry etching processes and is comparable to values reported in other ALE studies,⁵⁷⁻⁵⁹ highlighting the potential for this process to achieve high-fidelity, uniform etching over wafer-scale dimensions.

Conclusions

In summary, we have developed a highly precise and reproducible etching process for SiO_2 by combining sequential SF_6 gas exposure with Ar plasma at room temperature. The process achieves a stable EPC of $\sim 1.4 \text{ \AA}/\text{cycle}$, with 100% synergy confirmed between the modification and removal half-reactions. Parameter studies revealed well-defined process windows for temperature and ICP power, while saturation behavior and physisorption-dominated reversibility were confirmed through dose-dependent experiments. Mechanistic insights obtained via AIMD and DFT simulations highlight the role of surface defects as active sites for SF_6 dissociation and F adsorption. These findings support a model of the etching process involving both reversible physical adsorption and defect-mediated chemical adsorption. Moreover, directional etching was experimentally verified using pillar and hole structures. Uniformity testing over a 4.5 cm \times 4.5 cm area demonstrated high reproducibility with only 3.96% variation after 150 cycles. Importantly, the process relies on commercial RIE equipment and widely available gases, making it scalable and industrially compatible. Although demonstrated here for SiO_2 , the concept could be extended to other materials that exhibit selective reactivity between neutral gas-phase species

and plasma-generated radicals, opening pathways for broader applications in nanoscale fabrication. DOI: 10.1039/D5TC03428K

Author contributions

J.P. proposed the concepts and designed the experiments; V.R. and J.P. performed the experiments and analyzation; R.N. performed the MD and DFT calculation; R.Z. supervised the study; R.B. provided infrastructure to conduct the experiments; J.P., V.R., and R.Z. co-wrote the manuscript. All authors discussed the experimental and theoretical results and commented on the manuscript. All authors have approved the final version of the manuscript.

Acknowledgements

This work was funded by the Deutsche Forschungsgemeinschaft (DFG, German Research Foundation) – Projektnummer 192346071 – SFB 986 “Tailor-Made Multi-Scale Materials Systems”. The authors acknowledge the use of the Hamburg-CRR cleanroom facility, jointly operated by the University of Hamburg (UHH), DESY, and the Max Planck Institute for the Structure and Dynamics of Matter (MPSD), which was instrumental to the experimental work presented in this study. We also acknowledge support from the BMBF ForLab initiative. Nian Ran acknowledges funding from the National Natural Science Foundation of China (NSFC, Grant No. 22403103) and the Shanghai Sailing Program (Grant No. 23YF1454900). The authors thank Dr. Paul Plate, Dr. Michael Höfner, and Dr. Marcel Schulze (SENTECH Instruments GmbH) for valuable discussions and for providing Ar plasma characterization data used in this work.

Conflicts of interest

There are no conflicts to declare.

Data availability

The data supporting the findings of this work are available within the article and its Supplementary Information files. All other relevant data supporting the findings of this study are available from the corresponding author on request.

References

1. V. Cremers, R. L. Puurunen and J. Dendooven, *Applied Physics Reviews*, 2019, **6**, 021302.
2. A. Fischer, A. Routzahn, S. M. George and T. Lill, *Journal of Vacuum Science & Technology A*, 2021, **39**, 030801.
3. T. Faraz, F. Roozeboom, H. C. M. Knoops and W. M. M. Kessels, *ECS Journal of Solid State Science and Technology*, 2015, **4**, N5023.
4. J. Peng and R. Zierold, in *Encyclopedia of Condensed Matter Physics (Second Edition)*, ed. T. Chakraborty, Academic Press, Oxford, 2024, DOI:

COMMUNICATION

Journal Name

5. <https://doi.org/10.1016/B978-0-323-90800-9.00206-7>, pp. 716-728.

6. N. P. de Leon, K. M. Itoh, D. Kim, K. K. Mehta, T. E. Northup, H. Paik, B. S. Palmer, N. Samarth, S. Sangtawesin and D. W. Steuerman, *Science*, 2021, **372**, eabb2823.

7. W. Lu, Y. Lee, J. C. Gertsch, J. A. Murdzek, A. S. Cavanagh, L. Kong, J. A. del Alamo and S. M. George, *Nano Letters*, 2019, **19**, 5159-5166.

8. A. P. M. Place, L. V. H. Rodgers, P. Mundada, B. M. Smitham, M. Fitzpatrick, Z. Leng, A. Premkumar, J. Bryon, A. Vrajitoarea, S. Sussman, G. Cheng, T. Madhavan, H. K. Babla, X. H. Le, Y. Gang, B. Jäck, A. Gyenis, N. Yao, R. J. Cava, N. P. de Leon and A. A. Houck, *Nature Communications*, 2021, **12**, 1779.

9. Z. Chen, I. M. Grace, S. L. Woltering, L. Chen, A. Gee, J. Baugh, G. A. D. Briggs, L. Bogani, J. A. Mol, C. J. Lambert, H. L. Anderson and J. O. Thomas, *Nature Nanotechnology*, 2024, **19**, 986-992.

10. C. Y. Chen, Z. Sun, R. Torsi, K. Wang, J. Kachian, B. Liu, G. B. Rayner, Z. Chen, J. Appenzeller, Y.-C. Lin and J. A. Robinson, *Nature Communications*, 2024, **15**, 4016.

11. K. J. Kanarik, T. Lill, E. A. Hudson, S. Sriraman, S. Tan, J. Marks, V. Vahedi and R. A. Gottscho, *Journal of Vacuum Science & Technology A*, 2015, **33**, 020802.

12. K. J. Kanarik, S. Tan and R. A. Gottscho, *The Journal of Physical Chemistry Letters*, 2018, **9**, 4814-4821.

13. X. Chen, H.-R. Park, M. Pelton, X. Piao, N. C. Lindquist, H. Im, Y. J. Kim, J. S. Ahn, K. J. Ahn, N. Park, D.-S. Kim and S.-H. Oh, *Nature Communications*, 2013, **4**, 2361. 1988.

14. T.-Y. Lee, P.-T. Chen, C.-C. Huang, H.-C. Chen, L.-Y. Chen, P.-T. Lee, F.-C. Chen, R.-H. Horng and H.-C. Kuo, *Nanoscale Advances*, 2025, **7**, 2796-2817.

15. Y. Lee and S. M. George, *ACS Nano*, 2015, **9**, 2061-2070.

16. T. Lill, *Atomic layer processing: semiconductor dry etching technology*, 2021.

17. J. W. DuMont, A. E. Marquardt, A. M. Cano and S. M. George, *ACS Applied Materials & Interfaces*, 2017, **9**, 10296-10307.

18. D. Catherall, A. Hossain and A. Minnich, *arXiv:2405.05491*, 2024, DOI: 10.48550/arXiv.2405.05491.

19. N. Miyoshi, K. Shinoda, H. Kobayashi, M. Kurihara, Y. Kouzuma and M. Izawa, *Journal of Vacuum Science & Technology A*, 2021, **39**, 052601.

20. R. Dussart, T. Tillicher, L. Becerra, P. Lefaucheux and L. J. Overzet, *Japanese Journal of Applied Physics*, 2025, **64**, 05SP01.

21. V. Bliznetsov, H. M. Lin, Y. J. Zhang and D. Johnson, *Journal of Micromechanics and Microengineering*, 2015, **25**, 087002.

22. S. F. Yoon, *Microelectronic Engineering*, 1991, **14**, 23-40.

23. R. Hsiao and J. Carr, *Materials Science and Engineering: B*, 1998, **52**, 63-77.

24. X. Man, N. Bao, Y. Hao, Y. Feng and X. Ma, *physica status solidi (a)*, 2020, **217**, 2000223.

25. S. Haugg, C. Hedrich, R. H. Blick and R. Zierold, *Nanomaterials*, 2021, **11**, 3357.

26. C. Hedrich, D. Deduystsche, R. R. Petit, T. Krekeler, J. Peng, M. Ritter, J. Dendooven, C. Detavernier, R. H. Blick and R. Zierold, *Surfaces and Interfaces*, 2025, **57**, 105696.

27. J. P. Perdew, K. Burke and M. Ernzerhof, *Physical Review Letters*, 1996, **77**, 3865-3868.

28. P. E. Blöchl, *Physical Review B*, 1994, **50**, 17953-17979. [View Article Online](https://doi.org/10.1103/PhysRevB.50.17953)

29. G. Kresse and J. Furthmüller, *Physical Review B*, 1996, **54**, 11169-11186.

30. A. Jain, S. P. Ong, G. Hautier, W. Chen, W. D. Richards, S. Dacek, S. Cholia, D. Gunter, D. Skinner, G. Ceder and K. A. Persson, *APL Materials*, 2013, **1**.

31. S. S. Kaler, Q. Lou, V. M. Donnelly and D. J. Economou, *Journal of Physics D: Applied Physics*, 2017, **50**, 234001.

32. R. J. Gasvoda, A. W. van de Steeg, R. Bhowmick, E. A. Hudson and S. Agarwal, *ACS Applied Materials & Interfaces*, 2017, **9**, 31067-31075.

33. K. Koh, Y. Kim, C.-K. Kim and H. Chae, *Journal of Vacuum Science & Technology A*, 2017, **36**, 01B106.

34. S. Dallorto, A. Goodyear, M. Cooke, J. E. Szornel, C. Ward, C. Kastl, A. Schwartzberg, I. W. Rangelow and S. Cabrini, *Plasma Processes and Polymers*, 2019, **16**, 1900051.

35. S. Dallorto, M. Lorenzon, J. Szornel, A. Schwartzberg, A. Goodyear, M. Cooke, M. Hofmann, I. W. Rangelow and S. Cabrini, *Journal of Vacuum Science & Technology B*, 2019, **37**.

36. S. Y. Kim, I.-S. Park and J. Ahn, *Applied Surface Science*, 2022, **589**, 153045.

37. Y. S. Lee, S. J. Kim, J. J. Lee, C. H. Cho, I. H. Seong and S. J. You, *Journal of Physics D: Applied Physics*, 2022, **55**, 365203.

38. Y. Kim, H. Kang, C. Kim and H. Chae, *ACS Sustainable Chemistry & Engineering*, 2023, **11**, 6136-6142.

39. A. Osonio, T. Tsutsumi, B. Mukherjee, R. Borude, N. Kobayashi and M. Hori, *Japanese Journal of Applied Physics*, 2023, **62**, 121001.

40. J. Kim, H. Kang, Y. Kim, M. Jeon and H. Chae, *Plasma Processes and Polymers*, 2024, **21**, 2300216.

41. R. J. Gasvoda, Y. G. P. Verstappen, S. Wang, E. A. Hudson and S. Agarwal, *Journal of Vacuum Science & Technology A*, 2019, **37**, 051003.

42. N. Miyoshi, H. Kobayashi, K. Shinoda, M. Kurihara, K. Kawamura, Y. Kouzuma and M. Izawa, *Journal of Vacuum Science & Technology A*, 2021, **40**, 012601.

43. K. J. Kanarik, S. Tan, W. Yang, T. Kim, T. Lill, A. Kabansky, E. A. Hudson, T. Ohba, K. Nojiri, J. Yu, R. Wise, I. L. Berry, Y. Pan, J. Marks and R. A. Gottscho, *Journal of Vacuum Science & Technology A*, 2017, **35**.

44. V. Miikkulainen, M. Leskelä, M. Ritala and R. L. Puurunen, *Journal of Applied Physics*, 2013, **113**, 021301.

45. K. S. W. Sing, *Pure and Applied Chemistry*, 1985, **57**, 603-619.

46. A. D. Kulkarni, D. G. Truhlar, S. Goverapet Srinivasan, A. C. T. van Duin, P. Norman and T. E. Schwartzentruber, *The Journal of Physical Chemistry C*, 2013, **117**, 258-269.

47. V. A. RADZIG, in *Defects in SiO₂ and Related Dielectrics: Science and Technology*, eds. G. Pacchioni, L. Skuja and D. L. Griscom, Springer Netherlands, Dordrecht, 2000, DOI: 10.1007/978-94-010-0944-7_12, pp. 339-370.

48. P. Norman and T. E. Schwartzentruber, presented in part at the LAMMPS Users' Workshop and Symposium, 2011.

49. R. Dronskowski and P. E. Blöchl, *The Journal of Physical Chemistry*, 1993, **97**, 8617-8624.

50. R. Knizikevičius, *Vacuum*, 2009, **83**, 953-957.

51. Y. A. Mankelevich, E. N. Voronina, T. V. Rakhimova, A. P. Palov, D. V. Lopaev, S. M. Zyryanov and M. R. Baklanov, *The European Physical Journal D*, 2017, **71**, 126.



Journal Name

COMMUNICATION

52. H. Pedersen, S. T. Barry and J. Sundqvist, *Journal of Vacuum Science & Technology A*, 2021, **39**.

53. S. Shi, Y. Li, Z. Cui, Y. Yan, X. Zhang, J. Tang and S. Xiao, *Chemical Engineering Journal*, 2023, **470**, 144166.

54. G. S. Oehrlein, S. M. Brandstatter, R. L. Bruce, J. P. Chang, J. C. DeMott, V. M. Donnelly, R. Dussart, A. Fischer, R. A. Gottscho, S. Hamaguchi, M. Honda, M. Hori, K. Ishikawa, S. G. Jaloviar, K. J. Kanarik, K. Karahashi, A. Ko, H. Kothari, N. Kuboi, M. J. Kushner, T. Lill, P. Luan, A. Mesbah, E. Miller, S. Nath, Y. Ohya, M. Omura, C. Park, J. Poulose, S. Rauf, M. Sekine, T. G. Smith, N. Stafford, T. Standaert and P. L. G. Ventzek, *Journal of Vacuum Science & Technology B*, 2024, **42**. New Article Online DOI: 10.1039/D5TC03428K

55. M. Teichmann, J. Lorbeer, F. Frost and B. Rauschenbach, *Nanoscale Research Letters*, 2014, **9**, 439.

56. H. Winter, *Physics Reports*, 2002, **367**, 387-582.

57. K. J. Kanarik, T. Lill, E. A. Hudson, S. Sriraman, S. Tan, J. Marks, V. Vahedi and R. A. Gottscho, *Journal of Vacuum Science & Technology A*, 2015, **33**.

58. M. Huff, *Micromachines*, 2021, **12**, 991.

59. US12272530B2, 2025.



Figures and Figure Captions

View Article Online

DOI: 10.1039/D5TC03428K

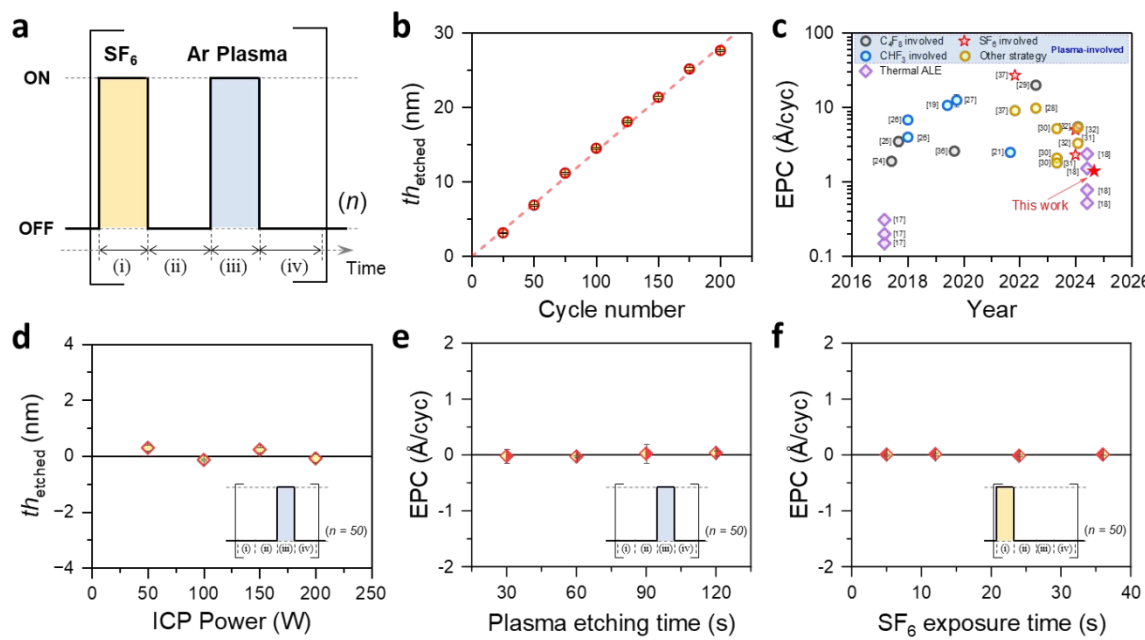


Figure 1. Process configuration and synergy validation. (a) Schematic of the cyclic etching process comprising n sequential cycles. Each cycle includes four steps: (i) SF₆ exposure, (ii) Purge, (iii) Ar plasma etching and (iv) Cleaning purge. (b) The EPC determined to be ~ 1.4 Å/cycle based on a linear fitting with $R^2 \approx 0.999$ of etched thickness, th_{etched} , versus cycle number of the standard loop recipe. The numbers adjacent to data points correspond to literature references. (d) A blank period replaces step (i) in the standard recipe. The ICP power is changed in step (iii), indicating that Ar plasma cannot etch SiO₂ by sputtering within this power range. (e, f) Synergy validation by replacing either step (i) or (iii) in the standard process with a blank period. No etching is observed when either half-reaction is applied independently, confirming that etching only occurs when both steps are combined, indicative of 100% synergy.

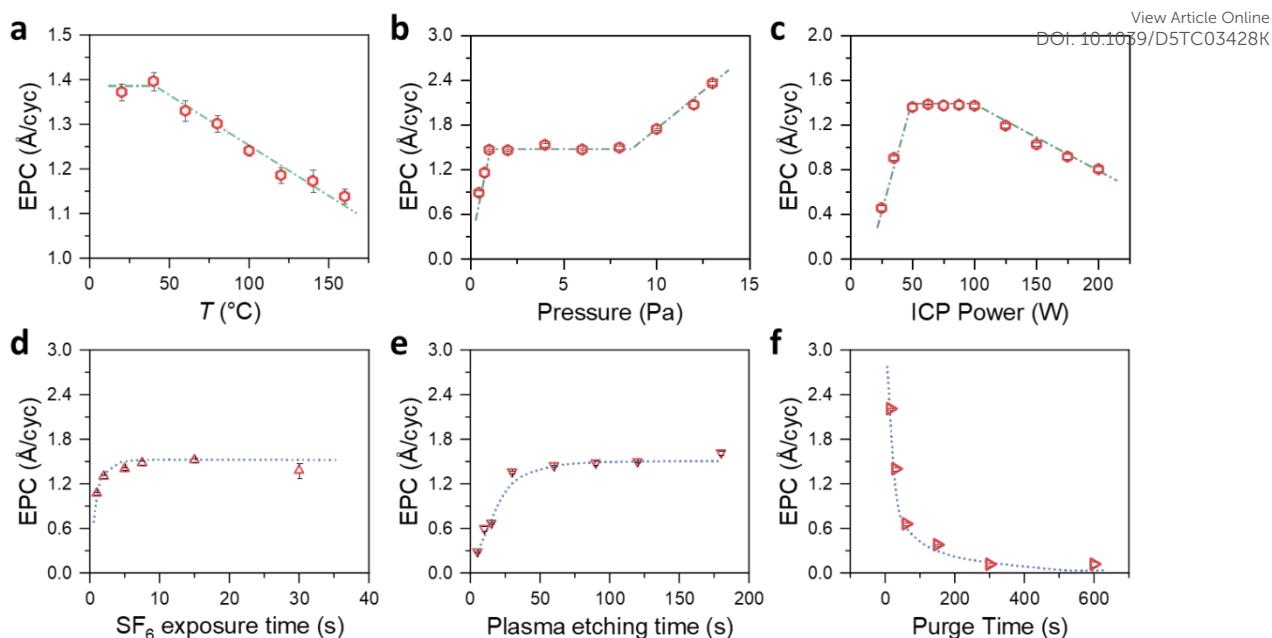


Figure 2. Etching characteristics under single-parameter variations. (a–c) Process windows are identified in which the EPC remains stable when varying (a) wafer holder temperature, (b) chamber pressure, and (c) ICP power. These plateaus indicate the self-limiting behavior. As the (d) SF₆ exposure time and (e) the plasma etching duration increases, the EPC gradually approached saturation. The phenomena in (d) and (e) exhibit conventional ALE-like self-limitation characteristics. (f) However, as the purge time in step (ii) prolongs, the EPC drops dramatically and then approaches a no-etching state gradually, suggesting physical absorption of SF₆ in step (i).



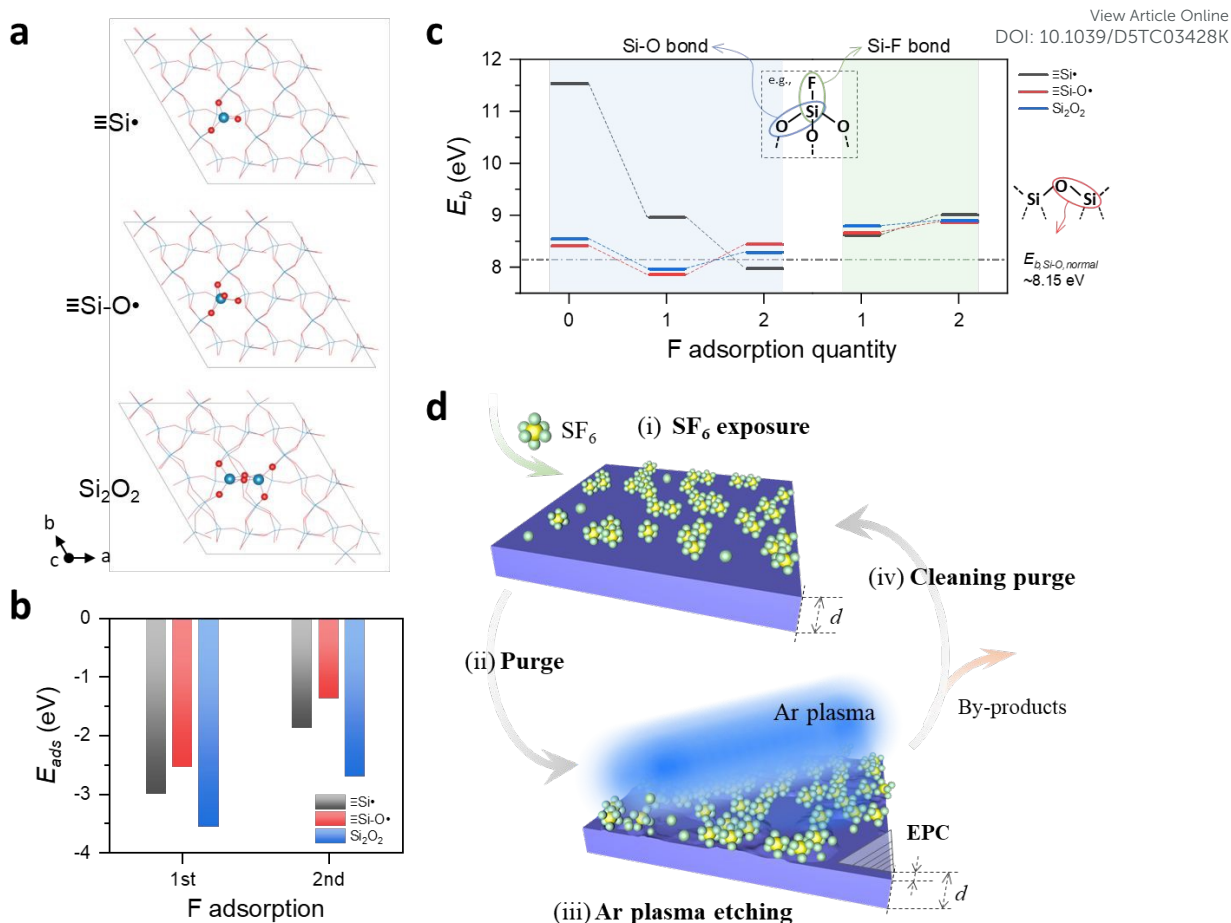


Figure 3. Mechanistic insights into the etching process. (a) Three dominant surface defects on SiO_2 surface. (b) The adsorption energy E_{ads} for the different surface defects to F atoms. All negative E_{ads} values indicate that the reaction occurs spontaneously. (c) Comparison of bonding strength, E_b , for Si-O and Si-F as the F adsorption quantity. The black dashed line represents the Si-O bond strength in defect-free regime on the surface, $E_{b,\text{Si}-\text{O},\text{normal}}$. Insets: A $\equiv\text{Si}\cdot$ defect with one F adsorbed as an example of Si-O and Si-F studied; Si-O bond on defect-free surface regime. (d) Schematic of the proposed etching mechanism using sequential SF_6 gas exposure and pulsed Ar plasma. Unlike conventional ALE, this process combines both chemical adsorption at reactive defect sites and reversible physical adsorption in the step (i) SF_6 exposure, contributing to etching during the step (iv) Ar plasma step.

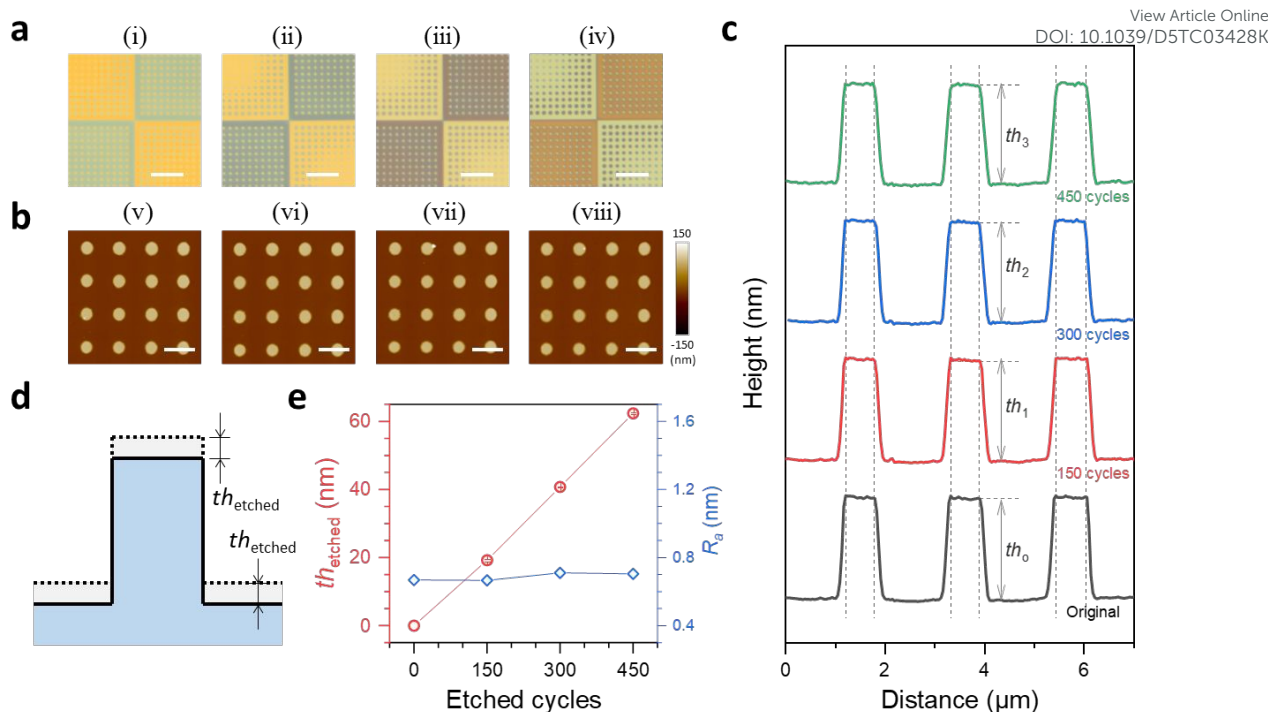


Figure 4. Directional etching. Pillar structures were used to evaluate the anisotropy of the etching process. (a) Optical microscope images and (b) the corresponding AFM images of the original pillar sample (i, v), the same position after 150 etching cycles (ii, vi), the same position after 300 etching cycles (iii, vii), and the same position after 450 etching cycles (iv, viii). The color variation is due to the different thicknesses of SiO_2 after etching. The scalebar for (a) and (b) are 10 μm and 2 μm , respectively. (c) Height profiles of three consecutive pillars in their original state and after 150, 300, and 450 etching cycles. The corresponding pillar heights th_0 , th_1 , th_2 , and th_3 are 91.4 ± 1.17 , 91.3 ± 0.86 , 90.7 ± 0.91 , 89.6 ± 1.00 nm, respectively, which keeps the same during the etching. (d) Sketch of the directional etching result. (e) Corresponding etched thickness th_{etched} and roughness R_a during the test as a function of cycle number. The stable and low R_a suggests a damage-free and uniform etching process.

Data availability statement

The data supporting this article have been included as part of the Supplementary Information.